

[Click here to view linked References](#)

## 200 Insights into the mechanochemical synthesis of Sn- $\beta$ : solid-state metal incorporation in beta zeolite

Hrishikesh Joshi,<sup>1</sup> Cristina Ochoa-Hernández,<sup>1</sup> Edward Nürenberg,<sup>1</sup> Liqun Kang,<sup>2</sup> Feng Ryan Wang,<sup>2</sup> Claudia Weidenthaler,<sup>1</sup> Wolfgang Schmidt,<sup>1</sup> Ferdi Schüth<sup>1,\*</sup>

<sup>1</sup> Department of Heterogeneous Catalysis, Max-Planck-Institut für Kohlenforschung, Germany

<sup>2</sup> Department of Chemical Engineering, University College London, United Kingdom

### Abstract

Sn- $\beta$  zeolite is an active material for the isomerization of glucose to fructose, which is one of the critical reactions for the valorization of biomass. The material is synthesized either by a top-down or bottom-up approach<sup>66</sup>. In this work, we use a top-down approach for the synthesis of Sn- $\beta$  to incorporate the tin atoms into the \*BEA framework. As compared to the literature, we replace the process of manual grinding with the use of ball milling to make the process reproducible, flexible, and scalable. The primary focus of this work is to investigate the processes occurring during the synthesis by a variety of characterization tools. These techniques include thermogravimetric analysis (TGA), X-ray photoelectron spectroscopy (XPS), X-ray absorption spectroscopy (XAS), physisorption, X-ray diffraction (XRD), and chemisorption monitored by Fourier-transform infrared spectroscopy (FTIR). The synthesis is followed by characterizing the material at various stages of synthesis. Finally, the materials are tested for the isomerization of glucose to fructose to assess the chemical nature of Sn- $\beta$  zeolites. The results of this investigation provide several insights into the mechanochemical process for the incorporation of atoms in a zeolite framework. For instance, the importance of the size of precursors, distribution of Sn atoms during synthesis, and chemical changes occurring during milling are highlighted. These insights could produce a blueprint for the synthesis of a variety of solid catalysts.

**Keywords:** Sn-beta zeolite, solid-state reactions, metal incorporation, mechanochemistry, biomass conversion

## 1. Introduction

Mechanochemistry is a field of chemistry that deals with reactions under the influence of mechanical energy. Historically, in 1919 Ostwald coined the term mechanochemistry as a part of the chemical systematics together with thermochemistry, photochemistry, and electrochemistry. Though the first mechanochemical reaction is hard to trace,<sup>1</sup> Ostwald's inclusion of the term in his work marked the beginning of mechanochemistry as a new branch in chemistry. The current definition of mechanochemistry, as given by the IUPAC, is "a chemical reaction that is induced by the direct absorption of mechanical energy." This definition highlights the essential aspect of mechanochemistry, which is the activation of a substance that occurs due to the mechanical forces. The activation generally occurs in a microscopic environment at the site of collision within a fraction of seconds. This activation can result in various reactions with sufficient time and under suitable conditions. Mechanochemistry is currently receiving a high level of attention due to its ability to perform reactions under robust, scalable, and benign conditions. In materials science, this allows the development of new methods for phase transformations, nanoparticle formation, alloy formation, and ion exchange, to name a few.<sup>2</sup> Most of the early mechanochemical reactions in the field of solid catalyst development were performed by grinding solid materials together to form new compounds. Ion exchange or solid-state incorporations can be considered as the direct descendants of these reactions.

Incorporation of metal ions into a zeolite framework can be used to tune the properties of the host framework for desired reactions.<sup>3-5</sup> Sn- $\beta$  zeolite, which catalyzes the isomerization of glucose *via* its Lewis acid sites, is one such example.<sup>6</sup> Besides isomerization, Sn- $\beta$  can be used as a catalyst for dehydration, retro-aldol reactions, Meerwein-Ponndorf-Verley reduction (MPV), and Baeyer-Villiger oxidation reactions.<sup>3, 7-9</sup> Several methods have been developed for the synthesis of Sn- $\beta$ , which can be broadly classified into two classes, post-synthesis strategies (top-down) and hydrothermal methods (bottom-up).<sup>7, 10-13</sup> Moliner *et al.* demonstrated the hydrothermal synthesis of Sn- $\beta$  and its use for glucose isomerization reactions in 2010.<sup>6</sup> The synthesis was performed *via* a bottom-up approach by introducing Sn salts in the synthesis mixture before the hydrothermal step. Thermochemical post-synthetic methods are one of the top-down pathways used for the incorporation of cations into the zeolite frameworks. The synthesis is usually performed with solvents, where hydrolysis of the precursor and its subsequent insertion are the two main mechanistic

steps of the synthesis. In the case of Sn- $\beta$ , dealuminated beta zeolite acts as a host framework that incorporates the Sn cations following a thermochemical treatment.<sup>14</sup> Several groups have studied the effect of pore topology and parameters on these methods.<sup>15</sup> Recently, Bates *et al.* studied the reactivity of Sn substituted zeolites for a variety of zeolite frameworks. A vital feature of this work is that it discusses the various hypotheses revolving around the nature of Sn active sites.<sup>7</sup> In addition to Sn, several other metals can be inserted in a zeolite framework such as Hf, Ti, Ge, and Zr.<sup>5, 16</sup> The resulting Lewis acid zeolites are essential catalysts for biomass conversion.<sup>17</sup> Hammond *et al.* demonstrated the mechanochemical synthesis of Sn- $\beta$  in the year 2012.<sup>18</sup> The procedure they reported involves two steps, first grinding of dealuminated beta zeolite and Sn(CH<sub>3</sub>COO)<sub>2</sub>, and second, heat treatment of the composite. The group characterized the final material in detail to identify the nature of Sn incorporated in the framework.<sup>18, 19</sup> The reported method creates uniformly distributed Sn sites in the framework and also some SnO<sub>2</sub> nanoparticles. This solid-state metal incorporation performed under the influence of mechanical forces offers various advantages, such as eliminating the need for solvents.<sup>18</sup> We modified this approach by using ball milling instead of manual grinding. The use of milling makes the synthesis scalable, flexible, and reproducible by reducing manual errors. Moreover, parameters like energy transfer and temperature can be monitored closely to facilitate the scale-up of the synthesis process.<sup>20</sup> The reports in the literature on Sn- $\beta$  focus primarily on characterizing the active sites due to the complexity in the coordination environment. For most of these reports, samples were synthesized thermochemically, and so the correlation between synthesis parameters and the final active site provides information on the mechanism for only these methods.<sup>21, 22</sup> The studies that report solid-state methods for syntheses provide very little information on the mechanism of the synthesis, and in most cases, only the final states are characterized.<sup>19</sup> Therefore, in this work, we have investigated the details of solid-state incorporation of Sn into beta zeolite.

Furthermore, there are also questions concerning the possible fit of the tin-ions in the zeolite framework. The synthesis reported in literature uses the Sn<sup>2+</sup> cation (Sn(CH<sub>3</sub>COO)<sub>2</sub>), which has a radius of 118 pm.<sup>23</sup> This large cation cannot fit in the framework of beta zeolite based on the radii of the host framework ions (size of Si<sup>4+</sup> is 40 pm, and Al<sup>3+</sup> is 53 pm). Hence, it was speculated that the thermal treatment might lead to oxidation of the Sn<sup>2+</sup> to Sn<sup>4+</sup>, which could permit the incorporation of Sn into

the framework - the size of  $\text{Sn}^{4+}$  is 69 pm. This is still large for isomorphous incorporation into the beta framework, with a coordination number of 4. However, several reports have proposed that water molecules are coordinated on the Sn to increase its coordination number and permit the Sn to fit inside the framework. The sizes quoted here are based on a fixed sphere model with oxide or fluoride anions and are thus not fully adequate for predicting the substitution behavior of atoms.<sup>24</sup> Therefore, these numbers should be used only as first approximation rules for substitution. However, considering these limitations, the size of  $\text{Sn}^{2+}$  is still too large for framework substitution. On the other hand, the size of  $\text{Sn}^{4+}$  might be small enough to allow insertion into the framework. One would thus expect that  $\text{Sn}^{4+}$  compounds would be better choices for incorporation, and the resulting materials should have higher activity for the isomerization reaction. Interestingly, our first experiments had revealed that the material synthesized with  $\text{Sn}(\text{CH}_3\text{COO})_4$  shows no activity for glucose isomerization even after increasing the shaking frequency and time for milling. Therefore, it was important to study in some more detail the processes occurring during synthesis, which could include hydrolysis, precursor dispersion, oxidation of Sn cation, and coordination of Sn with the beta zeolite. The investigation is carried out by characterizing the material at various stages of the synthesis with thermogravimetry, sorption analysis, XAS, XRD, and FTIR spectroscopy.

## **2. Experimental Section**

### **2.1 Materials**

Ethanol (EtOH, 99.8%), methyl isobutyl ketone, acetone, N,N-dimethylformamide, glucose, acetone- $d^6$ , hydrochloric acid, Sn(II)acetate ( $\text{Sn}(\text{CH}_3\text{COO})_2$ ), Sn(IV)acetate ( $\text{Sn}(\text{CH}_3\text{COO})_4$ ), Sn(IV)chloride ( $\text{SnCl}_4 \cdot 5\text{H}_2\text{O}$ ), D-(+)-glucose, and tetraethoxysilane (TEOS, 98%) were purchased from Sigma Aldrich (Merck). Tetraethylammonium hydroxide (TEAOH, 40 % solution in water, Alfa Aesar), nitric acid ( $\text{HNO}_3$ ), ammonium hydroxide (25 wt %, VWR), and hydrofluoric acid (HF, aqueous, 40 %, Acros) was purchased from various companies as specified. All chemicals were used as received without further purification. Beta zeolite (H- $\beta$ ) with a Si/Al ratio of 35 was obtained from Südchemie (now Clariant).

### **2.2 Synthesis**

#### *2.2.1 Dealumination of H- $\beta$*

In a typical synthesis, 5 g of H- $\beta$  was suspended in 100 mL of conc. HNO<sub>3</sub> and refluxed at 80 °C for 8 h. After 8 h, the material was washed with water and centrifuged several times at 9000 rpm. The washing procedure was repeated until the pH of the supernatant solution was 7. The precipitate was dried in an oven at 90 °C to obtain the dealuminated beta zeolite (De- $\beta$ ). In one of the experiments, the dealumination was performed with conc. HCl ((Cl)De- $\beta$ ). The remaining procedure was the same as reported above for conc. HNO<sub>3</sub>.

### 2.2.2 Synthesis of Sn- $\beta$ by ball milling

**Table 1** describes the various types of materials synthesized by ball milling. In a typical process, the De- $\beta$  zeolite was activated under argon at 120 °C for 24 h and then 1 g of it was charged into a tungsten carbide (WC) milling jar (25 mL). An adequate amount of Sn precursor (e.g., 50 mg) and three 12 mm WC milling balls were added to the jar. The jar was then mounted on a shaker mill (Retsch MM400) and milled for the required time and with a fixed frequency. Further, the sample was heat-treated in an oven at 550 °C for 5 h (ramp rate 2 °C min<sup>-1</sup>). The parameters that were changed from the standard procedure (milling time of 20 min, shaking frequency of 10 Hz and heat treatment at 550 °C for 5 h) are indicated in the name of the sample.

<Table 1>

## 2.3 Characterization

Light scattering experiments were carried out on a Zetasizer® ZS Malvern® instrument for the determination of particle size. Typically, for particle size measurements (dynamic light scattering measurements), 2-5 mg mL<sup>-1</sup> of the sample was dispersed in water and measured in disposable 3 mL cuvettes. All measurements were performed in triplicates.

SEM micrographs and SEM-EDX mappings were recorded on a Hitachi S-5500, ultra high resolution scanning electron microscopy with a point resolution of 4 Å at 30 kV acceleration voltage. Bulk EDX measurements were performed on a Hitachi S-3500N electron microscope.

Physisorption measurements were carried out on a Micromeritics 3Flex instrument. Before the analysis, materials were activated under vacuum for at least 10 h at 300 °C. External specific surface areas and micropore volumes were determined from t-plots, using the Micromeritics 3Flex software package.

Thermogravimetric analysis coupled with mass spectrometry (TG-MS) was carried out on a Netzsch STA 449 F3 Jupiter thermal analysis instrument connected to a Netzsch QMS 403 D Aëolos mass spectrometer. Approximately 5 mg of sample was heated in 40 mL min<sup>-1</sup> gas flow (argon or synthetic air) with an additional protective flow of 20 mL min<sup>-1</sup> of argon. The heating rate was 10 °C min<sup>-1</sup> for a temperature range of 50-900 °C. Mass spectra were collected in scan mode.

FTIR spectra were recorded using a Nicolet iS50 FTIR spectrometer equipped with an MCT detector (128 scans at 4 cm<sup>-1</sup> resolution). Self-supported wafers (ca. 10 mg cm<sup>-2</sup>) of selected samples were activated under vacuum (10<sup>-3</sup>-10<sup>-4</sup> mbar) at 450 °C for 4 h. Then, pyridine (3 mbar) was adsorbed at 150 °C for 20 min. Thereafter, desorption was carried out at 150 °C for 20 min. The following bands and integrated molar extinction coefficients were used for quantification: a) samples containing aluminum<sup>25</sup>- Brønsted acid sites at 1545 cm<sup>-1</sup> and  $\epsilon = 1.67 \text{ cm } \mu\text{mol}^{-1}$ , Lewis acid sites at 1455 cm<sup>-1</sup> and  $\epsilon = 2.22 \text{ cm } \mu\text{mol}^{-1}$  and b) samples containing tin<sup>26</sup> - Brønsted acid sites at 1545 cm<sup>-1</sup> and  $\epsilon = 1.67 \text{ cm } \mu\text{mol}^{-1}$ , Lewis acid sites at 1452 cm<sup>-1</sup> and  $\epsilon = 1.42 \text{ cm } \mu\text{mol}^{-1}$ . For acetonitrile, self-supported wafers (ca. 10 mg cm<sup>-2</sup>) of selected samples were activated under vacuum (10<sup>-3</sup>-10<sup>-4</sup> mbar) at 450 °C for 4 h. The measurements were conducted at r.t. by dosing an adequate amount of CD<sub>3</sub>CN until saturation of the sample was achieved. Spectra were recorded after each dose, and after 20 min of desorption under vacuum. All FTIR measurements were performed in transmission mode.

XRD data were measured with a Stoe STADI P transmission diffractometer in Debye–Scherrer geometry. The instrument was equipped with a bent primary germanium monochromator allowing measurements with monochromatic CuK<sub>α1</sub> radiation. Diffracted intensities were recorded with a position-sensitive detector (PSD) made by Stoe. The PSD enables simultaneous recording of about 6° (2θ). Samples were measured in 0.7 mm borosilicate glass capillaries (wall thickness 0.01 mm) as dry powders.

Diffuse reflectance UV-Vis spectra of solid samples were recorded on a PerkinElmer Lambda 365 spectrophotometer equipped with an integrating sphere. BaSO<sub>4</sub> was used as a reference.

<sup>1</sup>H-NMR spectra of molecules in solution were measured at r.t. on an AV-300 spectrometer from Bruker. Chemical shifts are reported in parts per million (ppm) with the solvent residual peak as the internal standard. For solvent suppressed NMR, the

WET pulse sequences were used to suppress the solvent signals of acetone, water, and MIBK.

$^{119}\text{Sn}$  MAS NMR spectra were recorded on a Bruker Avance III HD 500WB spectrometer using a double-bearing MAS probe (DVT BL4) at a resonance frequency of 186.4 MHz. The spectra were measured by applying a Hahn-echo sequence with a  $\pi/2$ -pulse of 3.05  $\mu\text{s}$  and a pulse spacing of 100  $\mu\text{s}$  at a spinning rate of 10°kHz. High-power proton decoupling (tppm) was applied. At a recycle delay of 15/30 s between 3,200 and 16,000 scans were accumulated. The spectra were referenced with respect to  $\text{Si}(\text{CH}_3)_4$  using  $\text{SnO}_2$  as secondary reference ( $\delta = -604.3$  ppm).

Sn K-edge XAFS studies were performed on the P64 beamline for advanced X-ray absorption spectroscopy at DESY PETRA III (Hamburg, Germany).<sup>27</sup> The X-ray beam was generated from an undulator and introduced through a  $\text{Si}(311)$  double-crystal fixed-exit monochromator. Sample powders were ground with cellulose for dilution and pressed into 13 mm diameter pellets. All pellets were measured in transmission and fluorescence mode simultaneously using ion-chamber detectors and a passivated implanted planar silicon (PIPS) detector, respectively. The energy scan range was 29.0 to 30.2 keV with a resolution of 0.4 eV  $\text{step}^{-1}$ . The spectrum of each sample was measured three times and merged to improve the signal-to-noise ratio. The energy shift was calibrated using a standard Sn foil. Data were processed using Athena and Artemis software.<sup>28</sup> The amplitude reduction factor  $S_0^2$  was calculated from EXAFS analysis of the Sn foil and used as a fixed parameter for EXAFS fitting.

XPS measurements were performed with a spectrometer from SPECS GmbH equipped with a PHOIBOS 150 1D-DLD hemispherical energy analyzer. The monochromatized Al  $K_\alpha$  X-ray source ( $E=1486.6$  eV) was operated at 15 kV, 200W, and 14 kV, 100W. For the narrow scans, pass energies of 20 and 50 eV were applied. The medium area mode was used as lens mode. The base pressure during the experiment in the analysis chamber was  $5 \times 10^{-10}$  mbar. To account for charging effects, all spectra were referenced to Si  $2p$  at 103.5 eV.

### 3. Results and discussion

The overall process for synthesis is shown in **Figure 1**. It consists of three steps; first, the dealumination of commercial H- $\beta$  zeolite, second the solid-state incorporation by mechanical forces, and third a heat treatment to obtain the final Sn- $\beta$  material.

<Figure 1>

Dealumination was carried out with conc.  $\text{HNO}_3$ , by an approach that was adapted from the literature.<sup>29,30,31</sup> 50 mg  $\text{mL}^{-1}$  zeolite (H- $\beta$ ) was suspended in conc.  $\text{HNO}_3$  and refluxed overnight. The material was thoroughly washed with water and subsequently dried in an oven at 90 °C (De- $\beta$ ). The dealumination is required for two reasons, (a) to create silanol nests in the structure by creating empty T-sites and (b) to reduce the Brønsted and Lewis acidity of the zeolite arising from the aluminum. The increase in silanol density was confirmed by the FTIR spectra shown in **Figure 2a**. H- $\beta$  presents four hydroxyl stretching bands ( $\nu_{\text{OH}}$ ) at 3782, 3736,  $\sim$ 3669, and 3609  $\text{cm}^{-1}$  ascribed to the presence of low acidity hydroxyl groups bonded to extraframework aluminum such as AlOOH species, terminal silanols, Al-OH groups where the Al is partially attached to the framework (one or two chemical bonds) and acidic bridging Si-OH-Al groups, respectively.<sup>32, 33</sup> After dealumination, broad bands around 3520  $\text{cm}^{-1}$  can be assigned to the hydrogen-bonded hydroxyl groups due to the presence of defects sites (silanol nests).<sup>33, 34</sup> The disappearance of bands associated with Al species (3782, 3669 and 3609  $\text{cm}^{-1}$ ) and the appearance of the band at 3520  $\text{cm}^{-1}$  (De- $\beta$  and De- $\beta$ \_20min-nh) confirms that the dealuminated process was performed successfully. Integrated molar extinction coefficients are affected by the presence of H-bonding interactions; thus, no fully quantitative information can be derived from these spectra. However, semi-quantitative information on the population of silanols is accessible. The samples were activated under vacuum at 250 °C to eliminate the physisorbed water in the materials and measured at room temperature (r.t). The absence of the bending vibration band at 1630  $\text{cm}^{-1}$  ( $\delta_{\text{OH}}$ ) confirmed the removal of excess water.<sup>35</sup> The silanol population of the materials was semi-quantitatively compared by the area under the silanol bands ( $\nu_{\text{OH}}$ ), as described in **Table S1**. From these results, it is inferred that the De- $\beta$  and De- $\beta$ \_20min-nh contain a similar amount of silanol groups, which decreases substantially with the incorporation of Sn. Similar trend was also obtained by TG analysis (**Table S1**) by determining the silanol content, which were partially based on the Zhuravlev model.<sup>36</sup> The silanol amount in De- $\beta$  and Sn- $\beta$ -0.2 was *ca.* 3.6  $\text{mmol g}^{-1}$  and 1.6  $\text{mmol g}^{-1}$ , respectively. A decrease in silanol intensity was also observed for Sn- $\beta$ -0.2 as compared to the De- $\beta$  in their corresponding FTIR spectra. This decrease may indicate that the Sn occupies the empty T-sites within the De- $\beta$ , leading to the re-condensation of the framework.

Alternatively, the reduction might also be due to the thermal treatment used in the synthesis of Sn- $\beta$ -0.2, which could lead to dehydroxylation.

To assess the effects of milling on the structural properties of the zeolite, the beta zeolite (H- $\beta$ ) was subjected to mechanical forces with varying milling frequencies. Dynamic light scattering (DLS) was used to analyze the hydrodynamic sizes of the samples subjected to these forces. **Figure 2b** shows the particle size distribution of the samples measured for their suspension in water (3 mg mL<sup>-1</sup>). A frequency of 10 Hz causes minimal changes in the particle size distribution, whereas 20 Hz reduces the particle size extensively, leading to a bimodal particle size distribution. The energy transferred during milling at 10 Hz is not high enough to cause severe changes in particle size, as seen by the DLS experiments, which is in agreement with the simulation studies conducted using discrete-element methods (DEM).<sup>37-41</sup> The aim here was to preserve the particle shape of zeolites; therefore, a frequency of 10 Hz was chosen for the solid-state incorporation. **The influence of milling (10 Hz) on the particle size distribution of De- $\beta$  was also analyzed by DLS (Figure S2), which shows that the changes are minimal.**

Milling may be capable of creating more defect sites (silanol nests), which could be beneficial for the synthesis. Therefore, De- $\beta$  was milled at 10 Hz for 20 min and analyzed by FTIR to probe the changes occurring in the distribution of silanol groups. However, the FTIR spectrum of De- $\beta$  milled at 10 Hz for 20 min (De- $\beta$ \_20min-nh) showed minimal changes, which was also corroborated by TG analysis (**Table S1**). The differences were insignificant to indicate any changes in the total silanol content; however, a slight increase in the terminal silanol content was seen in the FTIR spectrum (**Figure 2a**).

<Figure 2>

The second step in the process is the most important one, which is the solid-state incorporation of the metal ions into the framework. The process is described in detail in the experimental section. The materials are named based on the amount of precursor added in the milling jar. For instance, the material synthesized with 50 mg of Sn(CH<sub>3</sub>COO)<sub>2</sub> is named "Sn- $\beta$ -0.2", as 0.2 mmol g<sup>-1</sup> of Sn is added. A "\*" is added to the name when Sn(CH<sub>3</sub>COO)<sub>4</sub> was used instead of Sn(CH<sub>3</sub>COO)<sub>2</sub> for the synthesis. Appropriate suffixes are added to the names when parameters of the standard

synthesis were varied or omitted, which are tabulated in the experimental section (**Table 1**).

Thermogravimetric analysis of a physical mixture (suffixed with \_0min-nh) and right after milling for 20 min (suffixed with "\_nh" as it is the state before heat treatment) was carried out, as shown in **Figure 3**. After milling, the exothermic peak of decomposition for both precursors shifts towards higher temperatures as compared to their corresponding physical mixtures.

<Figure 3>

The shift in the peak temperature for  $\text{Sn}(\text{CH}_3\text{COO})_2$  (38 °C) is higher than that for the  $\text{Sn}(\text{CH}_3\text{COO})_4$  (16 °C). The shift could be attributed to the thermal stabilization offered by the zeolite framework, and the difference in the shifts could be attributed to the difference in the dispersion of the two precursors during milling. There is ca. 0.1 wt.% of  $\text{H}_2\text{O}$  available in the milling jar based on the saturation pressure of water and 4 wt.% of silanols (2 wt.% of  $\text{H}_2\text{O}$ ) present during milling. This suggests that the hydrolysis of the precursor may not occur effectively due to the insufficient amount of water. Assuming that most of the precursor does not hydrolyze during milling, the molecular sizes of the two Sn precursors can be obtained from their crystal structures.<sup>42</sup> If precursor species diffuses as molecular units,  $\text{Sn}(\text{CH}_3\text{COO})_2$  (0.6 nm) would fit in the pores of the beta framework (0.7 nm) much better than the  $\text{Sn}(\text{CH}_3\text{COO})_4$  (1.5 nm). In the case of  $\text{Sn}(\text{CH}_3\text{COO})_4$ , the molecules can then occupy only the defect sites and spaces larger than 1.5 nm. These spatial restrictions cause the difference in the shift in the peak temperatures, due to the different extent of thermal stabilization.

Furthermore, these spatial restrictions would result in differences in the spatial location of Sn in the final materials, which could support the argument above. The spatial distribution of the Sn species in the final materials after heat treatment was analyzed by SEM-EDX. The samples were microtomed after dispersing them in a resin, and the corresponding elemental maps were obtained, as shown in **Figure 4**.

<Figure 4>

The EDX mapping for the microtomed Sn- $\beta$ -0.2 sample (synthesized with  $\text{Sn}(\text{CH}_3\text{COO})_2$ ) shows that the Sn is distributed uniformly in the bulk material, which suggests that tin occupies locations within the framework. The tin content in the microtomed Sn- $\beta$ -0.4 sample was marginally higher than Sn- $\beta$ -0.2, but not doubled.

However, the overall Sn content was doubled, as confirmed by SEM-EDX bulk quantification. This suggests that with *ca.* 0.2 mmol g<sup>-1</sup> loading of Sn precursor, most of the sites within the framework are occupied, and the majority of the additional Sn formed SnO<sub>2</sub> like species, outside the framework. The formation of SnO<sub>2</sub> species was confirmed by spot analysis of the bright areas in the maps. The elemental mapping for Sn-β-0.2\* showed no presence of Sn in the microtomed samples. Several slices were examined, but Sn was not found in any of the sliced particles. The bulk-EDX mappings of these samples showed the presence of Sn at discrete locations, which may arise from the formation of SnO<sub>2</sub> on the outer surface. Overall, the SEM-EDX analysis corroborates the argument that the distinct spatial distributions are caused by the differences in precursor dispersion.

Alternatively, it can be argued that the precursor dispersion may occur during the heat treatment step by thermal diffusion of atoms, and then the size of the precursor is irrelevant. During the heat treatment, the SnO<sub>2</sub> structure starts to form at 150 °C.<sup>43</sup> The surface diffusion of SnO<sub>2</sub> would begin at *ca.* 250 °C (Hüttig temperature), and this may allow the insertion of Sn from the surface into the empty T-sites of the framework.<sup>44</sup> However, in such a scenario, the distribution of Sn should be similar for both precursors, or Sn should at least be present in the framework in detectable amount for Sn-β-0.2\*. No experimental evidence was found to support these statements, which suggests that the dispersion of precursors by thermal diffusion is minimal. Therefore, the size of precursors becomes relevant, and the dispersion of precursors during milling is the primary cause for the distinct spatial distributions of Sn.

In the case of Sn-β-0.2\_nh, a high mass loss (~ 8 wt.%) is seen below 200 °C, as compared to its physical mixture (Sn-β-0.2\_0min-nh). This mass loss (**Figure 3**) can be predominantly attributed to the desorption of water, based on the DSC signals and coupled MS spectra. The desorption of water may occur due to (a) the condensation of the hydrolyzed precursors or (b) arise from the desorption of water coordinated onto the Sn site (similar to the structure shown in **Figure 1**). The mass loss associated with the condensation of hydrolyzed Sn(CH<sub>3</sub>COO)<sub>4</sub> should be higher than that for Sn(CH<sub>3</sub>COO)<sub>2</sub>, based on the stoichiometry of the hydrolysis reactions. However, in the case of Sn(CH<sub>3</sub>COO)<sub>4</sub> (Sn-β-0.2\*\_nh), the mass loss below 200 °C was lower than in the case of Sn(CH<sub>3</sub>COO)<sub>2</sub>. This suggests that for Sn(CH<sub>3</sub>COO)<sub>2</sub> (Sn-β-0.2\_nh), the extent of hydrolysis is higher or high amount of water is coordinated on the Sn site. For Sn-β-0.2\_nh, complete hydrolysis would result in *ca.* 1 wt.% loss

from the condensation of the hydrolyzed  $\text{Sn}(\text{CH}_3\text{COO})_2$ . Therefore, a significant part of the 8 wt.% loss can be ascribed to the coordination of water onto the Sn site. The driving force for the adsorption of water could be the insertion of Sn into the framework that requires additional ligands to stabilize the coordination environment of the Sn atom. For a successful insertion of  $\text{Sn}^{2+}$  into the framework, it must oxidize to  $\text{Sn}^{4+}$  during milling, as discussed before in the introduction.

The oxidation state of the Sn species was investigated using XPS. Primarily, three types of samples were analyzed, before milling, after milling and after heat treatment. As seen in **Table 2**, a shift of 1 eV was seen for the Sn 3d lines compared to the physical mixture. The oxidation state of the milled sample and the heat-treated sample are similar, which suggests that potential oxidation instead occurred during milling, not later in the heat treatment. The ratios of Sn/Si from XPS and SEM-EDX are quite similar, which suggests that the Sn precursors are uniformly distributed in the sample. However, XPS is a surface technique that can only probe *ca.* 2-5 nm of the sample in depth. XPS can thus only give information on the oxidation state of the surface atoms, so the bulk Sn could still be in the  $\text{Sn}^{2+}$  state.

<Table 2>

Thus, to corroborate the results suggesting the oxidation of  $\text{Sn}^{2+}$  cations, X-ray absorption fine structure (XAFS) was used to investigate the chemical nature of Sn in bulk. XAFS has been shown to probe the Sn environment in zeolites adequately.<sup>45, 46</sup> Since the X-ray absorption near-edge (XANES) spectra of the Sn K-edge may not be linearly proportional to the oxidation state to provide quantitative numbers,<sup>47</sup> the data will only be analyzed qualitatively. In this investigation, six samples were analyzed – (a) before milling (suffix "\_0min-nh"), (b) sample milled for 10 min (suffix "\_10min-nh"), (c) sample milled for 20 min (suffix "\_nh"), (d) heat-treated sample (no suffix) and two references, SnO and SnO<sub>2</sub>. XANES for all the samples are shown in **Figure 5a**. It can be seen from the edge shifts that after 10 min of milling,  $\text{Sn}^{2+}$  has completely oxidized to  $\text{Sn}^{4+}$ . For the physical mixture, the edge shift, seen in **Figure 5a**, could result from the partial oxidation of the sample.  $\text{Sn}(\text{CH}_3\text{COO})_2$  is not a stable compound, and the oxidation may be caused by mere mixing with the activated zeolite, forces applied during pellet pressing, or by air. Nevertheless, there is a significant shift in the edge energies of the samples before and after milling, which confirms the fact that the mechanical forces result in oxidation of  $\text{Sn}^{2+}$  to  $\text{Sn}^{4+}$ .

<Figure 5>

The  $k^2$ -weighted Fourier-transform (FT) EXAFS of samples (without phase correction) is shown in **Figure 5b**. The first coordination shell at around 2 Å is assigned to the Sn-O environment, while the Sn-Sn distance can be identified by the relatively intense features around 3.2 Å. The appearance of Sn-Sn distance indicates the formation of SnO<sub>2</sub>-like species. The EXAFS fitting results for the samples are shown in **Figure S3** and summarized in **Table 2**. The first shell coordination number increases from  $5.5 \pm 0.8$  to  $5.8 \pm 0.6$  after milling, which might be due to the coordination of water or hydroxyl ligands. After the heat treatment, a decrease in the Debye-Waller factor was observed, which may indicate the formation of defined Sn sites in more rigid environments – SnO<sub>2</sub> like species and Sn in the beta framework.

The oxidation of Sn cations may be facilitated by the presence of nitrates in the structure from the dealumination process. Therefore, a similar material was prepared, with the only difference that the HNO<sub>3</sub> was replaced with conc. HCl, as chloride ions are non-oxidizing. In this case, the oxidation was still observed (**Table 2**), which confirms that the oxidation is caused by the mechanical force with air as the oxidant. In summary, the XAFS and XPS analysis confirm the fact that mechanical forces oxidize the Sn<sup>2+</sup> to Sn<sup>4+</sup> in bulk, the coordination number of Sn increases slightly, possibly due to the coordination of water or hydroxyl ligands.

After heat treatment, two types of Sn sites are formed in the material: Sn incorporated in the framework and the oligomeric forms of tin resembling SnO<sub>2</sub>. The presence of both of these sites was confirmed by <sup>119</sup>Sn NMR and UV-Vis spectroscopy (**Figure S4-S5**). Resonance lines at -600 ppm can be attributed to the SnO<sub>2</sub>-type species and broad lines at -698 ppm to Sn incorporated in the framework. The <sup>119</sup>Sn NMR spectrum of a material synthesized *via* the hydrothermal route (Sn-β-hydro)<sup>9,48</sup> was also measured for comparison. For Sn-β-hydro, a resonance line at -725 ppm was observed, which was also attributed to the framework Sn. The synthesis is performed in a fluoride medium that causes the Sn<sup>4+</sup> cations to occupy different T-sites, which may lead to the shift in the line position.<sup>11</sup> **Sn-β-0.2 shows a resonance line at -698 ppm due to the absence of fluoride ions.** The bands at 250 nm in the UV-Vis spectra can be associated with SnO<sub>2</sub>, while the band at 220 nm can be ascribed to Sn in the framework.<sup>10</sup> The XRD patterns of the synthesized materials are shown in **Figure 6**. The XRD patterns of all the samples are similar to the reflections of the parent beta

structure (ICDD 48-0074). This may indicate that the crystal structure has not changed after the incorporation of Sn. Considering the crystal radii of Al, Si, and Sn atoms, this is unlikely as an observable change in lattice parameters would be expected. Alternatively, the structure may be disordered due to random stacking in the z-direction of the beta structure. This would result in a broadening of the reflections, and hence the shifts due to unit cell expansion might not be seen clearly. This fact was further confirmed by synthesizing highly crystalline Sn- $\beta$  samples (Sn- $\beta$ -hydro) with a more ordered structure, as reflected by the corresponding sharp reflections. Sn- $\beta$ -hydro showed an increase in d-spacing after the incorporation of Sn in the framework (**Figure 5, inset**). The crystallite size of the SnO<sub>2</sub> like species is probably very small, as the corresponding reflections are not observed for materials other than Sn- $\beta$ -0.8 and Sn- $\beta$ -0.2\* (**Figure 6**). Furthermore, the SnO<sub>2</sub> nanoparticles may not be highly crystalline, as the bands at 250 nm for Sn- $\beta$ -0.2\* were not observed in the UV-Vis spectra (**Figure S5**). The poor crystallinity of SnO<sub>2</sub> nanoparticles was confirmed by comparing it to crystalline SnO<sub>2</sub>: the XRD pattern of a physical mixture of De- $\beta$  and crystalline SnO<sub>2</sub> (0.2 mmol g<sup>-1</sup> of Sn) showed clear reflections for SnO<sub>2</sub>, which could be indexed to the cassiterite structure (ICDD 046-1088).

<Figure 6>

The textural properties of all samples are given in **Table S2**. The micropore volumes do not change upon the incorporation of Sn or removal of aluminum. Upon increasing the Sn precursor loading to *ca.* 0.8 mmol g<sup>-1</sup>, high amounts of SnO<sub>2</sub> would be formed, as expected from the SEM-EDX analysis. Indeed, this was confirmed by the XRD patterns, and by the decrease in micropore volume of Sn- $\beta$ -0.8 seen in **Table S2**. SnO<sub>2</sub> was also formed in the samples with a lower amount of Sn, but this did not have a significant influence on the micropore volumes. The external surface area of materials also remains similar for all samples, which suggests that the particle size does not change significantly after milling or heat treatment.

The final aspect of the characterization of the materials is the measurement of acidity and the chemical characterization of the Sn sites in the zeolite. It has been shown that framework and extra-framework sites react differently with glucose,<sup>49</sup> and hence it is crucial to identify the nature of the active sites. The Brønsted (B) and Lewis (L) acid sites were probed by a pyridine adsorption/desorption experiment, which was followed by FTIR (**Figure 7a**). The bands at 1545 cm<sup>-1</sup> (B) and 1455 cm<sup>-1</sup> (L) indicate

the existence of both types of acid sites in H- $\beta$ . Brønsted and Lewis acid sites are negligible in the De- $\beta$  sample, suggesting that the dealumination process was successful. After Sn incorporation (Sn- $\beta$ ), the Lewis acidity is proven by the appearance of the band at 1452  $\text{cm}^{-1}$ . Also, a very small amount of Brønsted acidity was observed and quantified. Concentrations of the acid sites are provided in **Table S2**.

In order to get further insights into the type of Lewis acid sites, acetonitrile ( $\text{CD}_3\text{CN}$ ) was used as a probe molecule and monitored by FTIR spectroscopy. Studies have shown that acetonitrile is capable of distinguishing two types of Sn Lewis acid sites, characterized by bands at 2316  $\text{cm}^{-1}$  and 2308  $\text{cm}^{-1}$ . The distinction can be made by gradually adding acetonitrile to the sample. The 2316  $\text{cm}^{-1}$  site is favored over the 2308  $\text{cm}^{-1}$  at low coverage, and upon increasing the amount of acetonitrile, the bands corresponding to both sites can be distinguished. In our case, these two separate bands upon gradual adsorption of acetonitrile were not observed (**Figure S6**). Instead, a redshift in the position of a single band was seen (from 2314  $\text{cm}^{-1}$  to 2310  $\text{cm}^{-1}$ ). After saturation of the adsorption sites, corroborated by the presence of physically adsorbed acetonitrile (2268  $\text{cm}^{-1}$ ), the excess acetonitrile was evacuated by applying a vacuum for 20 min at r.t. The  $\text{C}\equiv\text{N}$  stretching region of the final spectra are shown in **Figure 7b**. They depict a single broadband at ca. 2310  $\text{cm}^{-1}$  for Sn- $\beta$ -0.2 and Sn- $\beta$ -0.4. This result is similar to several reports on Sn- $\beta$  materials synthesized by a top-down approach, where only one band at ca. 2312  $\text{cm}^{-1}$  was observable.<sup>19</sup> The reason for the appearance of this non-resolvable band could be the heterogeneity in the crystal structure in terms of the environment around the active site. This heterogeneity probably arises due to the presence of disordered stacking in the beta structure, as mentioned before. Another broadband, possibly resulting from the convolution of two bands, is observed as illustrated in **Figure 7b**. The first band at 2286  $\text{cm}^{-1}$  could be attributed to the presence of double hydrolyzed Sn sites within the beta framework or the  $\text{SnO}_2$  species, as speculated by various reports. The second band located at 2275  $\text{cm}^{-1}$  could be ascribed to the acetonitrile H-bonded to Si-OH groups.<sup>7, 10, 13</sup>. In the case of the Sn- $\beta$ -0.2\*, no evidence of open or closed acid sites was found.

<Figure 7>

The identity of the sites giving rise to bands at 2316  $\text{cm}^{-1}$  and 2308  $\text{cm}^{-1}$  has remained a topic of great debate in the literature. Several groups have attempted to

identify the exact structure of these sites by using quantum chemical calculations.<sup>5, 11, 21</sup> Three kinds of proposed structures can explain the bands at 2316 cm<sup>-1</sup> and 2308 cm<sup>-1</sup>; (a) a closed-framework site (2308 cm<sup>-1</sup>), (b) an open-framework site (2316 cm<sup>-1</sup>), and (c) an open-defect site (2316 cm<sup>-1</sup>). The closed-framework site could be hydrolyzed to an open-framework site with sufficient amounts of water, and vice-versa regenerated upon dehydration.<sup>50</sup> It has been proposed that under measurement conditions (thermal activation and vacuum conditions), only open-defect site (2316 cm<sup>-1</sup>) and closed-framework (2308 cm<sup>-1</sup>) sites are probed. As the activation conditions can have a significant effect on the water/hydroxyl content in the sample, the interconversion of framework sites may be possible by varying these conditions. In our case (non-resolvable band), the interconversion would result in a redshift, as seen for the incremental dosing study. However, as seen in **Figure S7**, upon changing the activation conditions, the sites were not interconverted, as no shift in the bands was observed. In summary, our experiments confirm the proposals that under the FTIR chemisorption conditions, only the closed-framework site and open-defect site can be probed.

Further, the next step is to establish a correlation between the active sites and their reactivity. Several reports claim that for glucose isomerization, the 2316 cm<sup>-1</sup> site is more active (the open-framework and the open-defect sites) and for the ethanol dehydration, the 2308 cm<sup>-1</sup> (closed-framework) site is more active. Though the closed-framework sites are also probed in our measurement, it was sufficient to look at the entire area under the vibration bands at 2310 cm<sup>-1</sup>, because the open-defect sites and the closed sites, which will be converted to a hydrolyzed open site upon addition of water, are both active for the isomerization reaction.

The isomerization of glucose to fructose is an equilibrium ( $K_{\text{equilib}} \sim 1$ ) and a slightly endothermic reaction ( $\Delta H = 3 \text{ kJ mol}^{-1}$ ), which is catalyzed by Sn- $\beta$  zeolite, as reported by Moliner *et al.*<sup>6</sup> The catalysts synthesized in this work were tested for the isomerization to gain additional insights into the properties of the catalysts and to conclude on the processes during synthesis. A detailed description of the catalytic testing is provided in the supporting information. In brief, moderate-throughput batch reactions were conducted with a biphasic solvent system (MIBK and water), and the reaction mixture was analyzed by solvent suppressed NMR. An N<sub>2</sub> pressure of 10 bar was used to maintain an inert atmosphere. The final chemical compositions of the

reaction mixtures (**Figure 8**) were obtained to compare the catalytic activities of the catalysts.

The incorporation of Sn in the framework is vital for the isomerization, which can be verified by the negligible activity of H- $\beta$  and De- $\beta$  zeolites (**Figure 8, Entry 1-2**). The rate of the isomerization reaction is very fast, which is indicated by the small change in the final chemical composition between 2 h and 6 h reaction time (**Figure 8, Entry 3-5**). With prolonged time, fructose is converted to HMF due to the presence of a small amount of Brønsted acidity that was inferred from the pyridine chemisorption experiments. The yield of fructose shows a positive correlation to the amount of Sn up to 0.4 mmol g<sup>-1</sup> (Sn- $\beta$ -0.4); on a further increase, the yield of fructose does not increase substantially (**Figure 8, Entry 6-9**). This suggests that Sn- $\beta$ -0.8 contains a higher amount of SnO<sub>2</sub> nanoparticles, which are not active for the isomerization reaction, as also concluded from the XRD and electron microscopy data.

The heat treatment is an essential step of the synthesis. Sn- $\beta$ -0.4 was heat-treated at temperatures of 200 °C, 300 °C, 400 °C, and 550 °C. The resulting catalysts were tested for the isomerization reactions. The activity of catalysts showed a positive correlation to the heat treatment up to 550 °C (**Figure 8, Entry 13-16**). In order to test whether the temperature required for heat treatment could be reduced, the milling time in the synthesis was increased to 1 h. However, the sample milled for 1 h also required a heat treatment at 550 °C for high activity (**Figure 8, Entry 11-12**).

The catalyst synthesized with Sn(CH<sub>3</sub>COO)<sub>4</sub> (Sn- $\beta$ -0.2\*) did not show any activity for the isomerization reaction, as seen in **Figure 8, Entry 17**. This catalyst consists mainly of SnO<sub>2</sub> nanoparticles, which are not well crystallized and do not possess the active site based on acetonitrile chemisorption experiments, as discussed previously. The synthesis with Sn(CH<sub>3</sub>COO)<sub>4</sub> precursor was modified in an attempt to improve the incorporation by increasing the frequency or the time of milling. Both these materials did not show any activity for the isomerization at prolonged times of 16 h (**Figure 8, Entry 18-19**). Sn- $\beta$ -0.2\* does not form the active site due to the large size of the precursor, as established before in the material characterization part. To further support this hypothesis, materials were synthesized with Sn chloride precursors. The size of SnCl<sub>4</sub> is smaller than acetate, and so the metal incorporation should be successful in this case. Indeed, this was confirmed by the catalytic testing, where material synthesized by SnCl<sub>4</sub> had similar catalytic properties compared to

$\text{Sn}(\text{CH}_3\text{COO})_2$  (**Figure 8, Entry 20**). It thus seems to be the size and not the formal oxidation state of the precursor, which is crucial for forming the active site.

<Figure 8>

#### 4. Conclusions

In this work, the facile synthesis of Sn- $\beta$  zeolites by using ball milling was demonstrated. The method is based on the previously reported approach by Hammond *et al.* that used manual grinding. The main focus of our work was to study the mechanism of synthesis, and the changes that occur during the mechanochemical treatment. The first step of the synthesis, which is the dealumination of zeolite, creates empty T-sites by removing aluminum atoms from the framework. The absence of aluminum was confirmed by elemental analysis, pyridine adsorption studies, and the concurrent formation of silanol nests. The silanol nests are vital for the synthesis, as the Sn cation would then occupy these sites after the milling and heat treatment. The second step (mechanochemical treatment) was analyzed by XPS, XAFS, and thermogravimetric studies. The results suggest that during milling,  $\text{Sn}^{2+}$  is oxidized to  $\text{Sn}^{4+}$  in the presence of air. Further, due to the small molecular size of the  $\text{Sn}(\text{CH}_3\text{COO})_2$  precursor, it can reach the vacant T-sites in the structure and subsequently coordinate with the zeolite. During milling, a high amount of water (8 wt.%) is adsorbed, which is mostly coordinated to the Sn precursor at the T-site. The exact structure of the coordination is, however, difficult to determine with the current data. The effect of size was confirmed with precursors such as  $\text{Sn}(\text{CH}_3\text{COO})_4$ , which do not form active sites, as they cannot reach the T-sites within the pores. The final heat treatment in the synthesis is essential, and a temperature of 550 °C is necessary to attain the high activity for the isomerization reaction. The final material consists of Sn sites within the framework and  $\text{SnO}_2$  like species, as seen from XAFS, XRD and  $^{119}\text{Sn}$ -NMR. FTIR experiments using acetonitrile as a probe molecule were used to identify the type of Sn sites in the framework. Active sites were probed by observing the broad IR band of adsorbed acetonitrile at  $2310\text{ cm}^{-1}$ , but the identity of the different sites could not be resolved. However, for the isomerization reaction, all the sites would be active, and therefore, it is not necessary to distinguish these sites and quantify them individually. Overall, the mechanistic investigation of the process has revealed several features of the mechanochemical process that can be used for the synthesis of solid

catalysts. Further, the scalable, reproducible, solvent-free nature of this process makes it a highly attractive pathway for industrial implementations.

## Acknowledgments

H. Joshi would like to thank IMPRS-RECHARGE for financial support. The authors would like to thank H. Bongard for the SEM-EDX mapping of samples and S. Palm for the bulk EDX analysis. We acknowledge DESY PETRA III for the beamtime at the P64 beamline (Proposal ID: I-20190358 EC). We would like to thank W. Caliebe and V. Murzin for their assistance with the XAFS experiments. We would like to thank M. Leutzsch for the assistance with solvent suppressed NMR measurements and we would like to thank B. Zibrowius for the solid-state NMR measurements.

## References

1. Takacs, L., The historical development of mechanochemistry. *Chemical Society Reviews* **2013**, *42* (18), 7649-7659.
2. Balaz, P.; Achimovicova, M.; Balaz, M.; Billik, P.; Cherkezova-Zheleva, Z.; Criado, J. M.; Delogu, F.; Dutkova, E.; Gaffet, E.; Gotor, F. J.; Kumar, R.; Mitov, I.; Rojac, T.; Senna, M.; Streletskii, A.; Wieczorek-Ciurowa, K., Hallmarks of mechanochemistry: from nanoparticles to technology. *Chemical Society Reviews* **2013**, *42* (18), 7571-7637.
3. Dijkmans, J.; Dusselier, M.; Gabriëls, D.; Houthoofd, K.; Magusin, P. C. M. M.; Huang, S.; Pontikes, Y.; Trekels, M.; Vantomme, A.; Giebel, L.; Oswald, S.; Sels, B. F., Cooperative Catalysis for Multistep Biomass Conversion with Sn/Al Beta Zeolite. *ACS Catalysis* **2015**, *5* (2), 928-940.
4. Zhang, J.; Wang, L.; Wang, G.; Chen, F.; Zhu, J.; Wang, C.; Bian, C.; Pan, S.; Xiao, F.-S., Hierarchical Sn-Beta Zeolite Catalyst for the Conversion of Sugars to Alkyl Lactates. *ACS Sustainable Chemistry & Engineering* **2017**, *5* (4), 3123-3131.
5. Yang, G.; Zhou, L., Active Sites of M(IV)-incorporated Zeolites (M = Sn, Ti, Ge, Zr). *Scientific Reports* **2017**, *7* (1), 16113.
6. Moliner, M.; Roman-Leshkov, Y.; Davis, M. E., Tin-containing zeolites are highly active catalysts for the isomerization of glucose in water. *Proceedings of the National Academy of Sciences of the United States of America* **2010**, *107* (14), 6164-6168.
7. Bates, J. S.; Bukowski, B. C.; Harris, J. W.; Greeley, J.; Gounder, R., Distinct Catalytic Reactivity of Sn Substituted in Framework Locations and at Defect Grain Boundaries in Sn-Zeolites. *ACS Catalysis* **2019**, *9* (7), 6146-6168.
8. Corma, A.; Domine, M. E.; Nemeth, L.; Valencia, S., Al-free Sn-Beta zeolite as a catalyst for the selective reduction of carbonyl compounds (Meerwein-Ponndorf-Verley reaction). *Journal of American Chemical Society* **2002**, *124* (13), 3194-3195.

9. Corma, A.; Nemeth, L. T.; Renz, M.; Valencia, S., Sn-zeolite beta as a heterogeneous chemoselective catalyst for Baeyer-Villiger oxidations. *Nature* **2001**, *412* (6845), 423-425.
10. Dijkmans, J.; Dusselier, M.; Janssens, W.; Trekels, M.; Vantomme, A.; Breynaert, E.; Kirschhock, C.; Sels, B. F., An Inner-/Outer-Sphere Stabilized Sn Active Site in  $\beta$ -Zeolite: Spectroscopic Evidence and Kinetic Consequences. *ACS Catalysis* **2015**, *6* (1), 31-46.
11. Wolf, P.; Valla, M.; Núñez-Zarur, F.; Comas-Vives, A.; Rossini, A. J.; Firth, C.; Kallas, H.; Lesage, A.; Emsley, L.; Copéret, C.; Hermans, I., Correlating Synthetic Methods, Morphology, Atomic-Level Structure, and Catalytic Activity of Sn- $\beta$  Catalysts. *ACS Catalysis* **2016**, *6* (7), 4047-4063.
12. Sushkevich, V. L.; Ivanova, I. I.; Yakimov, A. V., Revisiting Acidity of SnBEA Catalysts by Combined Application of FTIR Spectroscopy of Different Probe Molecules. *The Journal of Physical Chemistry C* **2017**, *121* (21), 11437-11447.
13. Josephson, T. R.; Jenness, G. R.; Vlachos, D. G.; Caratzoulas, S., Distribution of open sites in Sn-Beta zeolite. *Microporous and Mesoporous Materials* **2017**, *245*, 45-50.
14. Tang, B.; Dai, W.; Wu, G.; Guan, N.; Li, L.; Hunger, M., Improved Postsynthesis Strategy to Sn-Beta Zeolites as Lewis Acid Catalysts for the Ring-Opening Hydration of Epoxides. *ACS Catalysis* **2014**, *4* (8), 2801-2810.
15. van der Graaff, W. N. P.; Tempelman, C. H. L.; Pidko, E. A.; Hensen, E. J. M., Influence of pore topology on synthesis and reactivity of Sn-modified zeolite catalysts for carbohydrate conversions. *Catalysis Science & Technology* **2017**, *7* (14), 3151-3162.
16. Iida, T.; Ohara, K.; Roman-Leshkov, Y.; Wakihara, T., Zeolites with isolated-framework and oligomeric-extraframework hafnium species characterized with pair distribution function analysis. *Phys Chem Chem Phys* **2018**, *20* (12), 7914-7919.
17. Luo, H. Y.; Lewis, J. D.; Roman-Leshkov, Y., Lewis Acid Zeolites for Biomass Conversion: Perspectives and Challenges on Reactivity, Synthesis, and Stability. *Annual Review of Chemical and Biomolecular Engineering* **2016**, *7*, 663-692.
18. Hammond, C.; Conrad, S.; Hermans, I., Simple and scalable preparation of highly active Lewis acidic Sn-beta. *Angewandte Chemie International Edition in English* **2012**, *51* (47), 11736-11739.
19. Hammond, C.; Padovan, D.; Al-Nayili, A.; Wells, P. P.; Gibson, E. K.; Dimitratos, N., Identification of Active and Spectator Sn Sites in Sn-beta Following Solid-State Stannation, and Consequences for Lewis Acid Catalysis. *ChemCatChem* **2015**, *7* (20), 3322-3331.
20. Santhanam, P. R.; Dreizin, E. L., Predicting conditions for scaled-up manufacturing of materials prepared by ball milling. *Powder Technology* **2012**, *221*, 403-411.
21. Bare, S. R.; Kelly, S. D.; Sinkler, W.; Low, J. J.; Modica, F. S.; Valencia, S.; Corma, A.; Nemeth, L. T., Uniform catalytic site in Sn-beta-zeolite determined using X-ray absorption fine structure. *Journal of American Chemical Society* **2005**, *127* (37), 12924-12932.
22. Boronat, M.; Concepcion, P.; Corma, A.; Renz, M.; Valencia, S., Determination of the catalytically active oxidation Lewis acid sites in Sn-beta zeolites, and their optimisation by the combination of theoretical and experimental studies. *Journal of Catalysis* **2005**, *234* (1), 111-118.

23. Stafeeva, V. S.; Mitiaev, A. S.; Abakumov, A. M.; Tsirlin, A. A.; Makarevich, A. M.; Antipov, E. V., Crystal structure and chemical bonding in tin(II) acetate. *Polyhedron* **2007**, *26* (18), 5365-5369.
24. Gibbs, G. V.; Ross, N. L.; Cox, D. F.; Rosso, K. M.; Iversen, B. B.; Spackman, M. A., Bonded radii and the contraction of the electron density of the oxygen atom by bonded interactions. *Journal of Physical Chemistry A* **2013**, *117* (7), 1632-1640.
25. Emeis, C. A., Determination of Integrated Molar Extinction Coefficients for Infrared Absorption Bands of Pyridine Adsorbed on Solid Acid Catalysts. *Journal of Catalysis* **1993**, *141* (2), 347-354.
26. Harris, J. W.; Cordon, M. J.; Di Iorio, J. R.; Vega-Vila, J. C.; Ribeiro, F. H.; Gounder, R., Titration and quantification of open and closed Lewis acid sites in Sn-Beta zeolites that catalyze glucose isomerization. *Journal of Catalysis* **2016**, *335*, 141-154.
27. Caliebe, W. A.; Murzin, V.; Kalinko, A.; Görlitz, M., High-flux XAFS-beamline P64 at PETRA III. *AIP Conference Proceedings* **2019**, *2054* (1), 060031.
28. Ravel, B.; Newville, M., ATHENA, ARTEMIS, HEPHAESTUS: data analysis for X-ray absorption spectroscopy using IFEFFIT. *Journal of Synchrotron Radiation* **2005**, *12* (Pt 4), 537-541.
29. Popovych, N. O.; Kyriienko, P. I.; Soloviev, S. O.; Orlyk, S. M.; Dzwigaj, S., Influence of partial dealumination of BEA zeolites on physicochemical and catalytic properties of AgAlSiBEA in H<sub>2</sub>-promoted SCR of NO with ethanol. *Microporous and Mesoporous Materials* **2016**, *226*, 10-18.
30. Yang, X.; Lv, B.; Lu, T.; Su, Y.; Zhou, L., Promotion effect of Mg on a post-synthesized Sn-Beta zeolite for the conversion of glucose to methyl lactate. *Catalysis Science & Technology* **2020**, *10* (3), 700-709.
31. Lami, E. B.; Fajula, F.; Anglerot, D.; Des Courieres, T., Single step dealumination of zeolite beta precursors for the preparation of hydrophobic adsorbents. *Microporous Materials* **1993**, *1* (4), 237-245.
32. Maache, M.; Janin, A.; Lavalley, J. C.; Joly, J. F.; Benazzi, E., Acidity of zeolites Beta dealuminated by acid leaching: An FTi.r. study using different probe molecules (pyridine, carbon monoxide). *Zeolites* **1993**, *13* (6), 419-426.
33. Omegna, A.; Vasic, M.; Anton van Bokhoven, J.; Pirngruber, G.; Prins, R., Dealumination and realumination of microcrystalline zeolite beta: an XRD, FTIR and quantitative multinuclear (MQ) MAS NMR study. *Physical Chemistry Chemical Physics* **2004**, *6* (2), 447-452.
34. Ide, M.; El-Roz, M.; De Canck, E.; Vicente, A.; Planckaert, T.; Bogaerts, T.; Van Driessche, I.; Lynen, F.; Van Speybroeck, V.; Thybault-Starzyk, F.; Van Der Voort, P., Quantification of silanol sites for the most common mesoporous ordered silicas and organosilicas: total versus accessible silanols. *Phys Chem Chem Phys* **2013**, *15* (2), 642-650.
35. Kawai, T.; Tsutsumi, K., A Study on the Surface Silanol Groups Developed by Hydrothermal and Acid Treatment of Faujasite Type Zeolites. *Journal of Colloid and Interface Science* **1999**, *212* (2), 310-316.
36. Zhuravlev, L. T., The surface chemistry of amorphous silica. Zhuravlev model. *Colloids and Surfaces A: Physicochemical and Engineering Aspects* **2000**, *173* (1-3), 1-38.

37. Chen, W.; Schoenitz, M.; Ward, T.; Dave, R. N.; Dreizin, E. L., Numerical Simulation of Mechanical Alloying in a Shaker Mill by Discrete Element Method. *KONA Powder and Particle Journal* **2005**, *23*, 152-162.
38. Colacino, E.; Carta, M.; Pia, G.; Porcheddu, A.; Ricci, P. C.; Delogu, F., Processing and Investigation Methods in Mechanochemical Kinetics. *ACS Omega* **2018**, *3* (8), 9196-9209.
39. Karthik, B.; Sai Gautam, G.; Karthikeyan, N. R.; Murty, B. S., Analysis of Mechanical Milling in Simoloyer: An Energy Modeling Approach. *Metallurgical and Materials Transactions A* **2011**, *43* (4), 1323-1327.
40. Magini, M.; Iasonna, A., Energy Transfer in Mechanical Alloying. *Materials Transactions, JIM* **1995**, *36* (2), 123-133.
41. Wang, M. H.; Yang, R. Y.; Yu, A. B., DEM investigation of energy distribution and particle breakage in tumbling ball mills. *Powder Technology* **2012**, *223*, 83-91.
42. Alcock, N. W.; Tracy, V. L., Acetates and acetato complexes. IV. The crystal and molecular structure of tin tetraacetate. *Acta Crystallographica Section B Structural Crystallography and Crystal Chemistry* **1979**, *35* (1), 80-83.
43. Kitabayashi, S.; Koga, N., Thermal Decomposition of Tin(II) Oxyhydroxide and Subsequent Oxidation in Air: Kinetic Deconvolution of Overlapping Heterogeneous Processes. *The Journal of Physical Chemistry C* **2015**, *119* (28), 16188-16199.
44. Moulijn, J. A.; van Diepen, A. E.; Kapteijn, F., Catalyst deactivation: is it predictable? *Applied Catalysis A: General* **2001**, *212* (1-2), 3-16.
45. Farges, F.; Linnen, R. L.; Brown, G. E., Redox and speciation of tin in hydrous silicate glasses: a comparison with Nb, Ta, Mo and W. *The Canadian Mineralogist* **2006**, *44* (3), 795-810.
46. Pelliccione, C. J.; Timofeeva, E. V.; Segre, C. U., Potential-Resolved In Situ X-ray Absorption Spectroscopy Study of Sn and SnO<sub>2</sub> Nanomaterial Anodes for Lithium-Ion Batteries. *The Journal of Physical Chemistry C* **2016**, *120* (10), 5331-5339.
47. Masai, H.; Ina, T.; Okumura, S.; Mibu, K., Validity of Valence Estimation of Dopants in Glasses using XANES Analysis. *Scientific Reports* **2018**, *8* (1), 415.
48. Corma, A.; Valencia, S. Stannosilicate molecular sieves. US Patent No. 5968473A. 1999.
49. Bermejo-Deval, R.; Gounder, R.; Davis, M. E., Framework and Extraframework Tin Sites in Zeolite Beta React Glucose Differently. *ACS Catalysis* **2012**, *2* (12), 2705-2713.
50. Qi, G.; Wang, Q.; Xu, J.; Wu, Q.; Wang, C.; Zhao, X.; Meng, X.; Xiao, F.; Deng, F., Direct observation of tin sites and their reversible interconversion in zeolites by solid-state NMR spectroscopy. *Communications Chemistry* **2018**, *1*, 22.

## Tables

**Table 1.** Parameters for the mechanochemical synthesis of materials.

Name <sup>a</sup>	De-β	Sn precursor - mg	Sn conc. <sup>b</sup>	Milling conditions		Heat treatment <sup>c</sup>
				mmol g <sup>-1</sup>	Hz	
Sn-β-0.2_0min-nh	1	Sn(CH <sub>3</sub> COO) <sub>2</sub> – 50	0.2	-	-	-
Sn-β-0.2_10min-nh	1	Sn(CH <sub>3</sub> COO) <sub>2</sub> – 50	0.2	10	10	-
Sn-β-0.2_nh	1	Sn(CH <sub>3</sub> COO) <sub>2</sub> – 50	0.2	10	20	-
Sn-β-0.2	1	Sn(CH <sub>3</sub> COO) <sub>2</sub> – 50	0.2	10	20	550 °C, 5 h
Sn-β-0.2_200°C	1	Sn(CH <sub>3</sub> COO) <sub>2</sub> – 50	0.2	10	20	200 °C, 5 h
Sn-β-0.2_300°C	1	Sn(CH <sub>3</sub> COO) <sub>2</sub> – 50	0.2	10	20	300 °C, 5 h
Sn-β-0.2_400°C	1	Sn(CH <sub>3</sub> COO) <sub>2</sub> – 50	0.2	10	20	400 °C, 5 h
Sn-β-0.1	1	Sn(CH <sub>3</sub> COO) <sub>2</sub> – 25	0.1	10	20	550 °C, 5 h
Sn-β-0.4	1	Sn(CH <sub>3</sub> COO) <sub>2</sub> – 100	0.4	10	20	550 °C, 5 h
Sn-β-0.8	1	Sn(CH <sub>3</sub> COO) <sub>2</sub> – 200	0.8	10	20	550 °C, 5 h
Sn-β-0.2*_0min-nh	1	Sn(CH <sub>3</sub> COO) <sub>4</sub> – 75	0.2	-	-	-
Sn-β-0.2*_nh	1	Sn(CH <sub>3</sub> COO) <sub>4</sub> – 75	0.2	10	20	-
Sn-β-0.2*	1	Sn(CH <sub>3</sub> COO) <sub>4</sub> – 75	0.2	10	20	550 °C, 5 h
Sn-β-0.2*_40min	1	Sn(CH <sub>3</sub> COO) <sub>4</sub> – 75	0.2	10	40	550 °C, 5 h
Sn-β-0.2*_15Hz	1	Sn(CH <sub>3</sub> COO) <sub>4</sub> – 75	0.2	15	20	550 °C, 5 h
Sn-β-0.3_Cl*	1	Sn(Cl) <sub>4</sub> .5H <sub>2</sub> O – 100	0.3	10	20	550 °C, 5 h
(Cl)Sn-β-0.2	1	Sn(CH <sub>3</sub> COO) <sub>2</sub> – 50	0.2	10	20	550 °C, 5 h

<sup>a</sup> "\*" indicates that Sn(CH<sub>3</sub>COO)<sub>4</sub> was used as the precursor, "Cl\*" indicates that SnCl<sub>4</sub>.5H<sub>2</sub>O was used as the precursor. "nh" – not heat treated. "(Cl)" – used dealuminated zeolite with conc. HCl for the synthesis of material.

<sup>b</sup> The concentrations are theoretical values and were also confirmed by bulk EDX analysis.

<sup>c</sup> The ramp rate used for all heat treatments was 2 °C min<sup>-1</sup>.

**Table 2.** Summary of XPS, EDX, and XAFS *ex-situ* characterization on various samples.

	XPS <sup>c</sup>			EDX	XAFS <sup>e</sup>			
	Sn 3d <sub>5/2</sub>	Sn 3d <sub>3/2</sub>	Sn <sup>d</sup> Si	Sn <sup>d</sup> Si	R	σ <sup>2</sup>	O.N.	C.N.
Sn-β-0.2_0min-nh <sup>a</sup>	487	495	6	-	2.06 (0.01)	7 (2)	+2, +4	5.5 (0.8)
Sn-β-0.2_10min-nh <sup>a</sup>	-	-	-	-	2.07 (0.02)	5 (2)	+4	5.8 (1.0)
Sn-β-0.2_nh <sup>a</sup>	488	496	1.3	1.3	2.05 (0.01)	6 (1)	+4	5.8 (0.6)
Sn-β-0.2 <sup>a</sup>	488	496	1.2	1.4	2.05 (0.01)	3 (1)	+4	6.3 (0.4)
SnO <sub>2</sub>	-	-	-	-	2.05	-	+4	6
(Cl)Sn-β-0.2 <sup>b</sup>	488	496	-	-	-	-	-	-

<sup>a</sup> These samples were prepared by using 1 g of De-β and 50 mg of Sn(CH<sub>3</sub>COO)<sub>2</sub> and then subjecting them to conditions as indicated in their name.

<sup>b</sup> The De-β zeolite used for this sample was prepared by a reflux treatment with HCl instead of HNO<sub>3</sub>.

<sup>c</sup> The measurements were referenced to the Si 2p peak (103.51 eV). Results expressed in eV.

<sup>d</sup> The Sn/Si ratio is reported in percentage.

<sup>e</sup> Bond length (R, Å), Debye-Waller factor (σ<sup>2</sup>) X 10<sup>3</sup>, oxidation number (O.N.), and coordination number (C.N.) for the Sn-O first shell coordination. Values in "()" are the errors associated with each parameter.

## Figure Captions

**Figure 1.** Schematic representation of the synthesis process. The first step removes the Al cations by chemical dealumination of the zeolite. The second step inserts the Sn cation into those positions by mechanochemical and thermal treatment. "x" represents the number of water molecules adsorbed on the Sn cation within the zeolite framework. Green, blue, brown, and orange balls represent aluminum, tin, silicon, and oxygen, respectively. Only three out of the four Si-O bonds are shown for simplicity.

**Figure 2.** (a) FTIR spectra of H- $\beta$ , De- $\beta$ , De- $\beta$ \_20min-nh, and Sn- $\beta$ -0.2 after activation at 250 °C for 6 h under vacuum to remove the physisorbed water. Spectra are plotted to show the OH stretching vibration region from 3800  $\text{cm}^{-1}$  - 3000  $\text{cm}^{-1}$ . (b) The hydrodynamic size distribution of H- $\beta$  milled for 20 min at various frequencies as indicated. A DLS instrument was used to measure the size of the materials in a suspension of water (3  $\text{mg mL}^{-1}$ ).

**Figure 3.** Thermogravimetric plots for samples, as indicated in the graph. The mixture samples were prepared by adding the required amount of precursor to De- $\beta$ , which are indicated by dotted lines. The temperature for the first exothermic peak was determined from the derivative of the TG curve (DTG), which corresponds to the highest exothermic weight loss. The peak temperature values and the endothermic H<sub>2</sub>O desorption region are indicated in the graph.

**Figure 4.** SEM-EDX maps of bulk samples (a-b, e-f, i-j) and microtomed samples (c-d, g-h, k-l) for Sn- $\beta$ -0.2, Sn- $\beta$ -0.4, and Sn- $\beta$ -0.2\*. The Si, O, and Sn atom% for each sample are provided on their respective graphs.

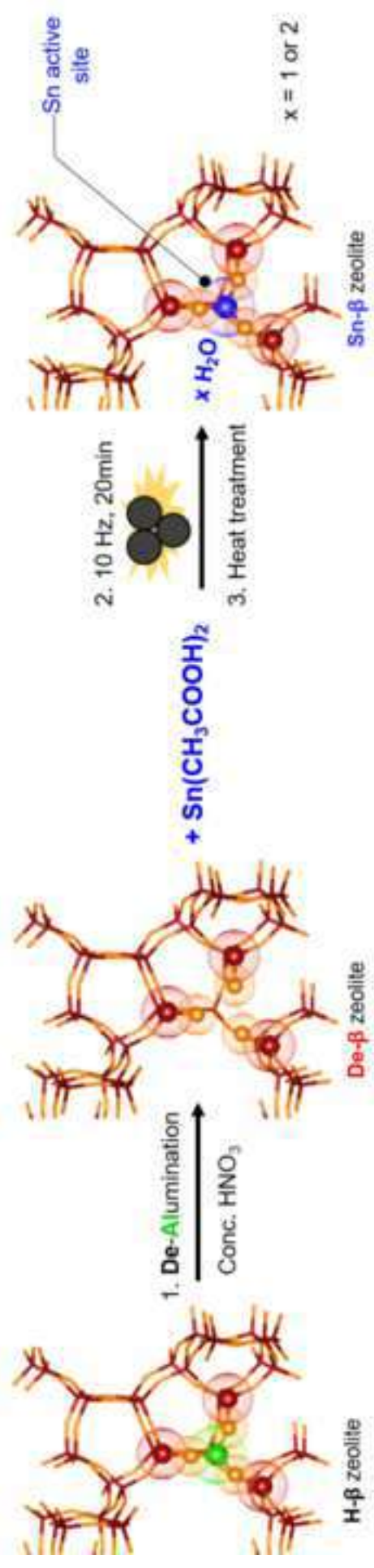
**Figure 5.** Sn K-edge (a) normalized XANES spectra (upper panel), their derivatives (lower panel), and (b)  $k^2$ -weighted Fourier transform of the spectra of Sn- $\beta$  at various stages of the synthesis - 0 min (physical mixture), milled for 10 min, milled for 20 min and heat-treated after milling. SnO, SnO<sub>2</sub>, and Sn foil were also measured as references and are plotted for comparison.

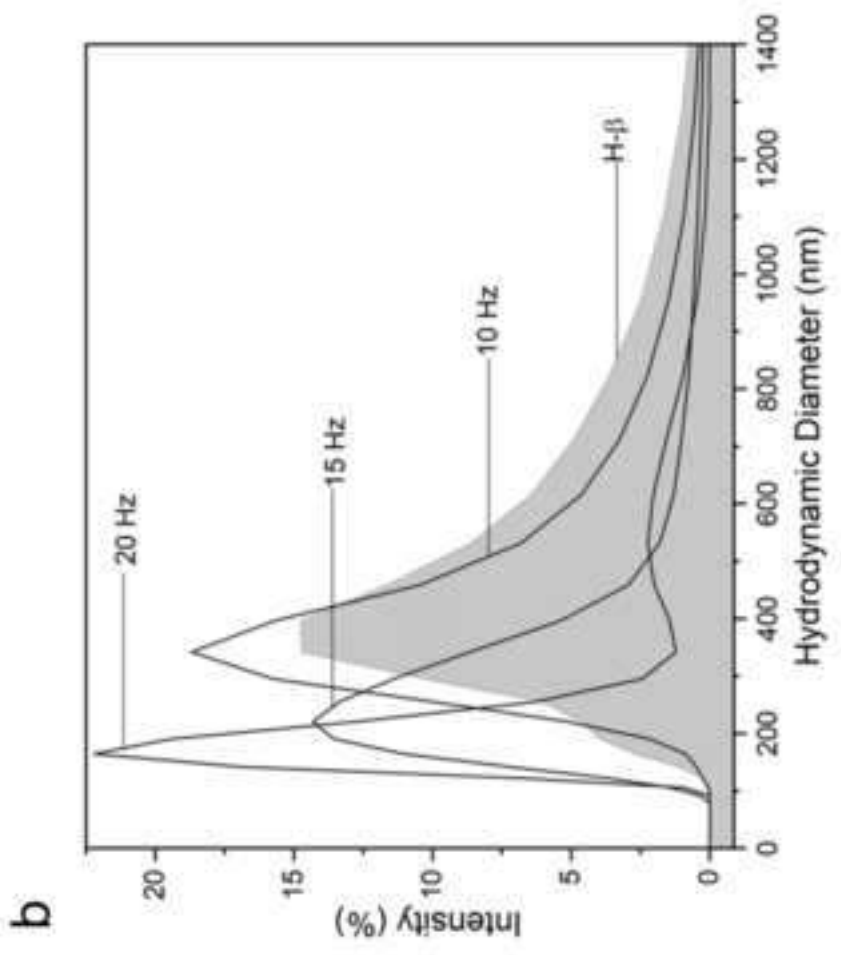
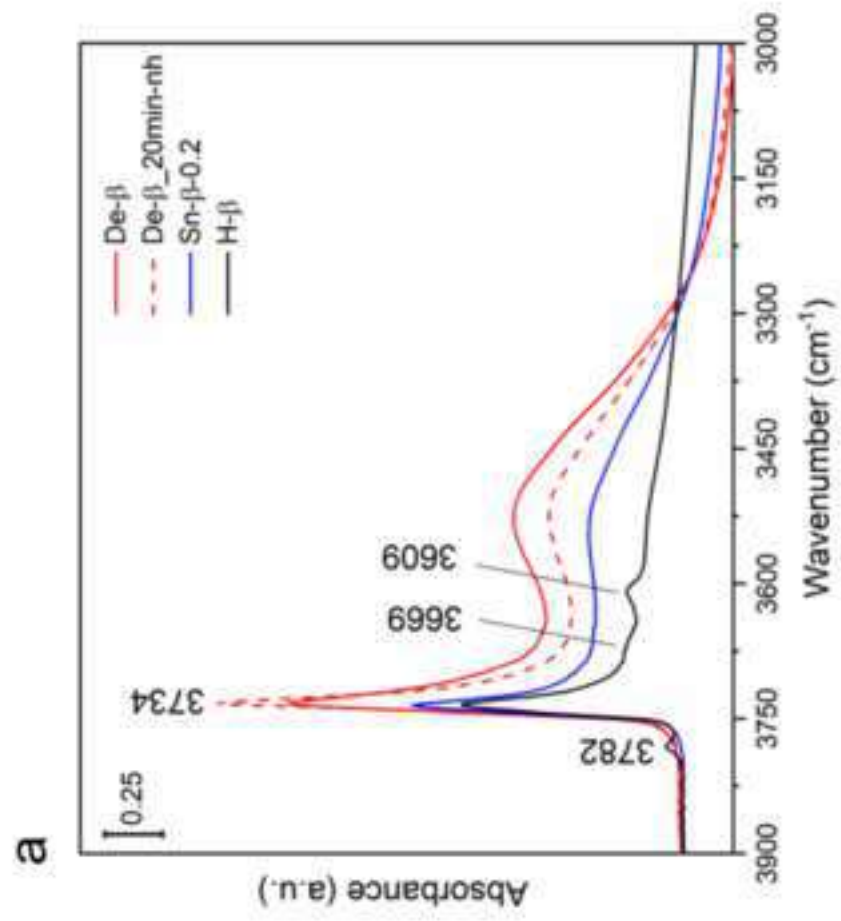
**Figure 6.** XRD diffraction patterns for H- $\beta$ , De- $\beta$ , Sn- $\beta$ -0.2, Sn- $\beta$ -0.4, Sn- $\beta$ -0.8, Sn- $\beta$ -0.2\*, physical mixture of SnO<sub>2</sub> and De- $\beta$  (1wt.% Sn), and Sn- $\beta$ -hydro. The reflections of SnO<sub>2</sub> (cassiterite) are shown in grey highlights and denoted by "s" in the graph. Inset graph: XRD patterns of H- $\beta$ , De- $\beta$ , Sn- $\beta$ -0.2, and Sn- $\beta$ -hydro to highlight the shift in reflection at  $2\theta = 22.5^\circ$ . All diffraction patterns have been normalized by the total area under the curves.

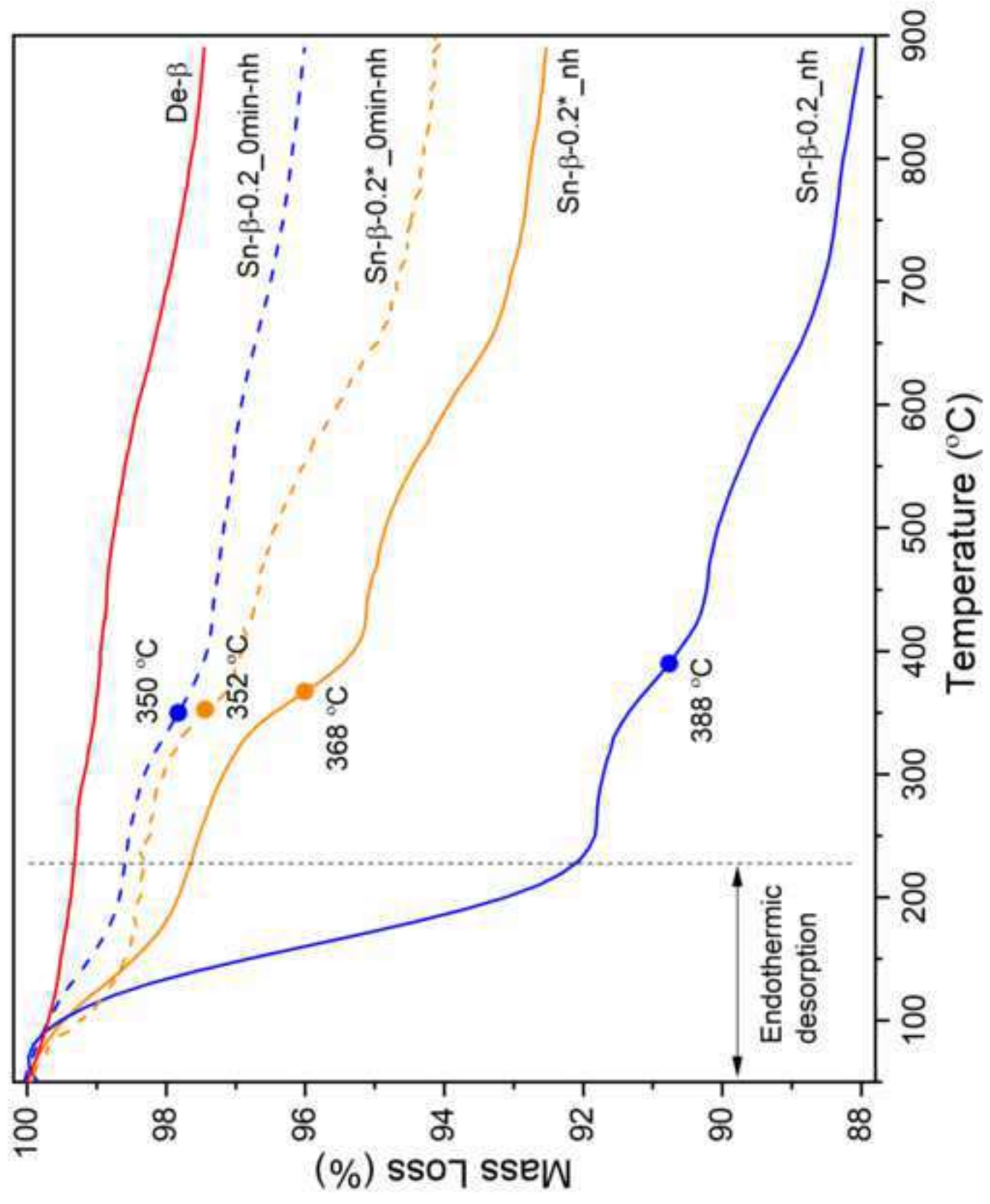
**Figure 7.** (a) FTIR spectra of pyridine adsorbed on Sn- $\beta$ -0.2, De- $\beta$ , and H- $\beta$  at 150 °C. (b) FTIR spectra of acetonitrile adsorbed on Sn- $\beta$ -0.4, Sn- $\beta$ -0.2, and Sn- $\beta$ -0.2\*. In all cases, the samples were activated under high temperature (450 °C) and vacuum

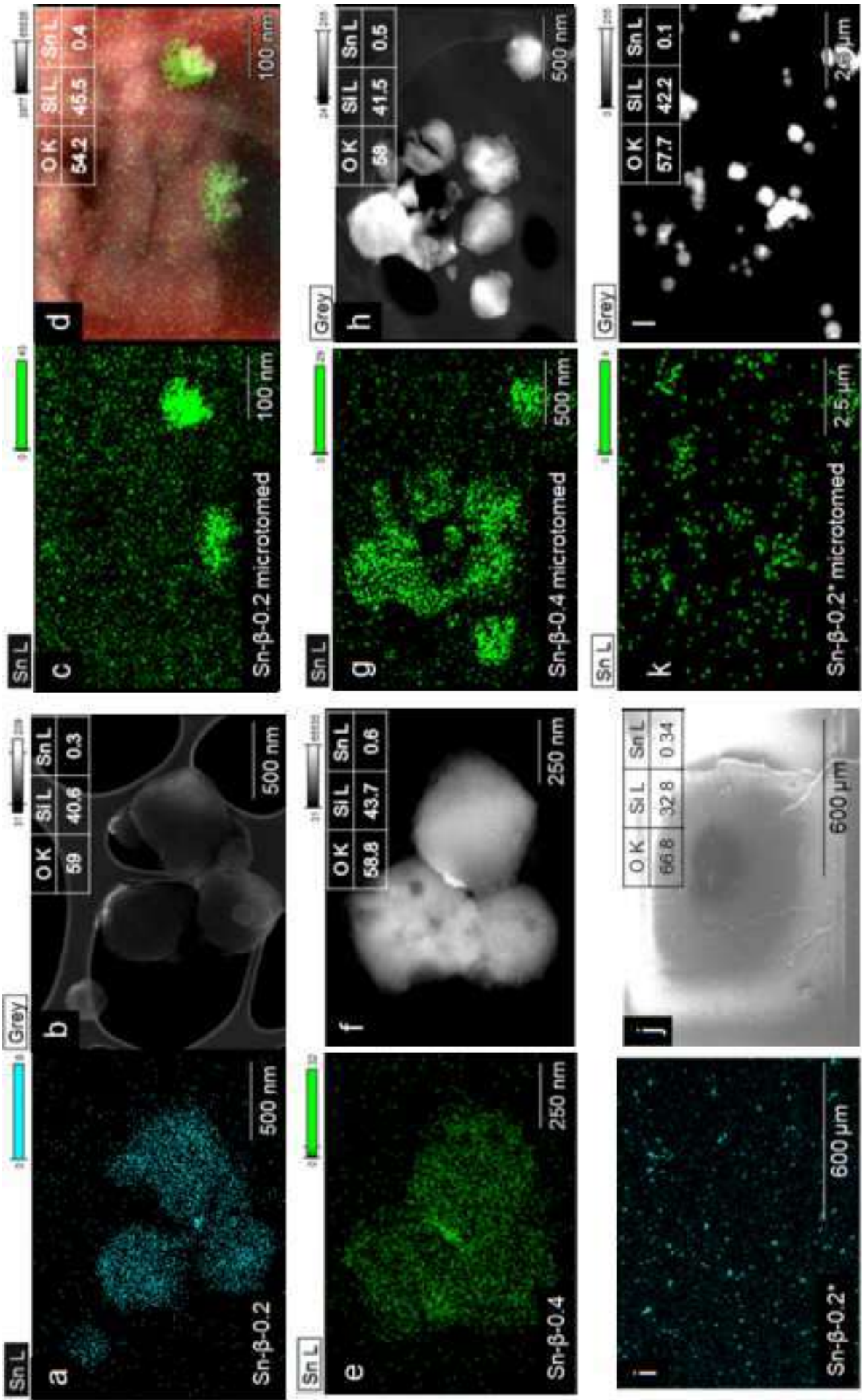
before dosing the pyridine or acetonitrile. The measurements were performed in transmission mode.

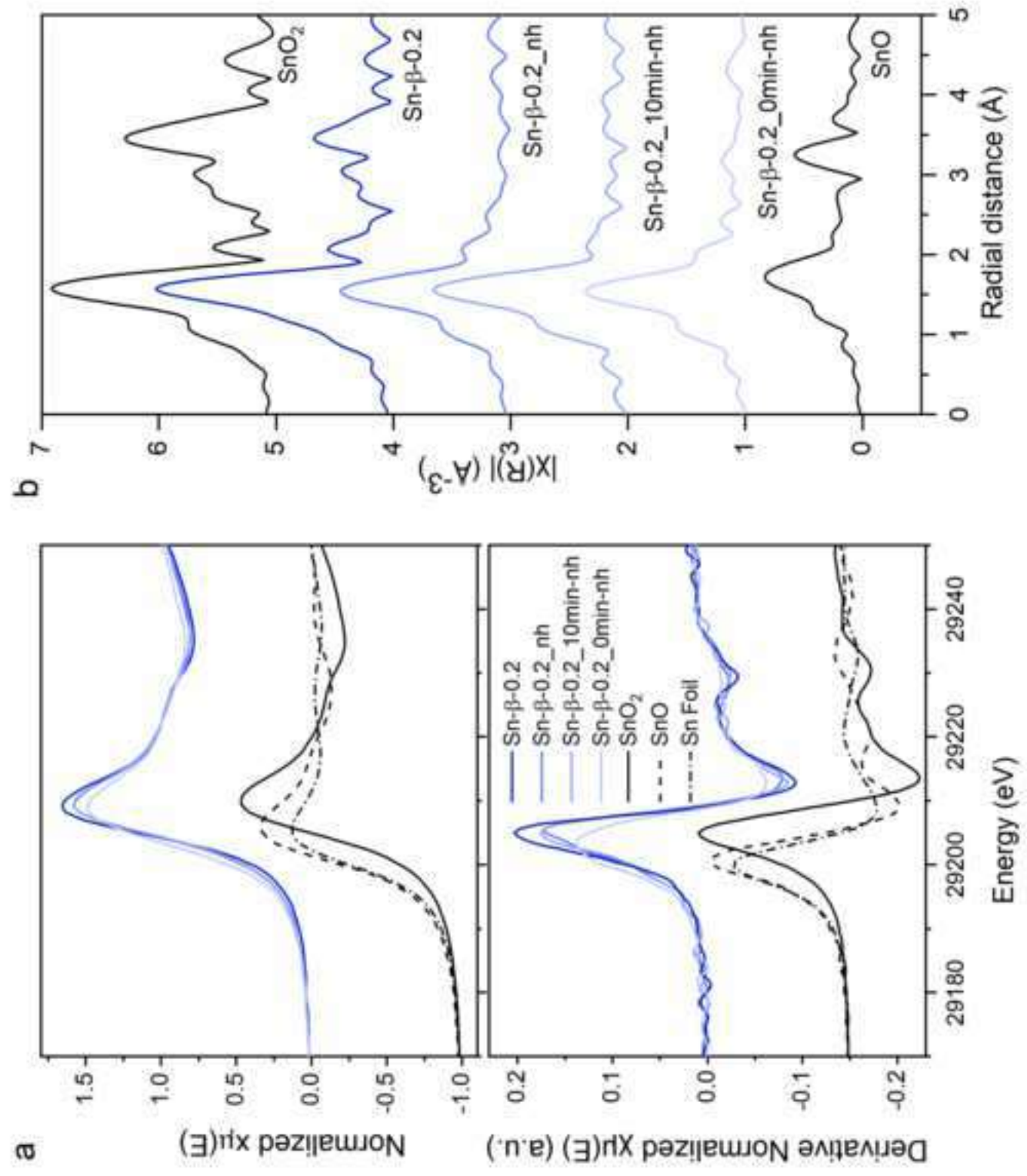
**Figure 8.** Catalytic test with 25 mg catalyst, water=2.5 mL, MIBK = 3.5 mL at a temperature of 140 °C. G indicates the type of gas, P = pressure (bar) of gas G at r.t. before reaction, t = time of reaction in h, and 0.7 mmoles of glucose were used as the reactant. Black/grey – glucose, blue- fructose, and green – HMF.

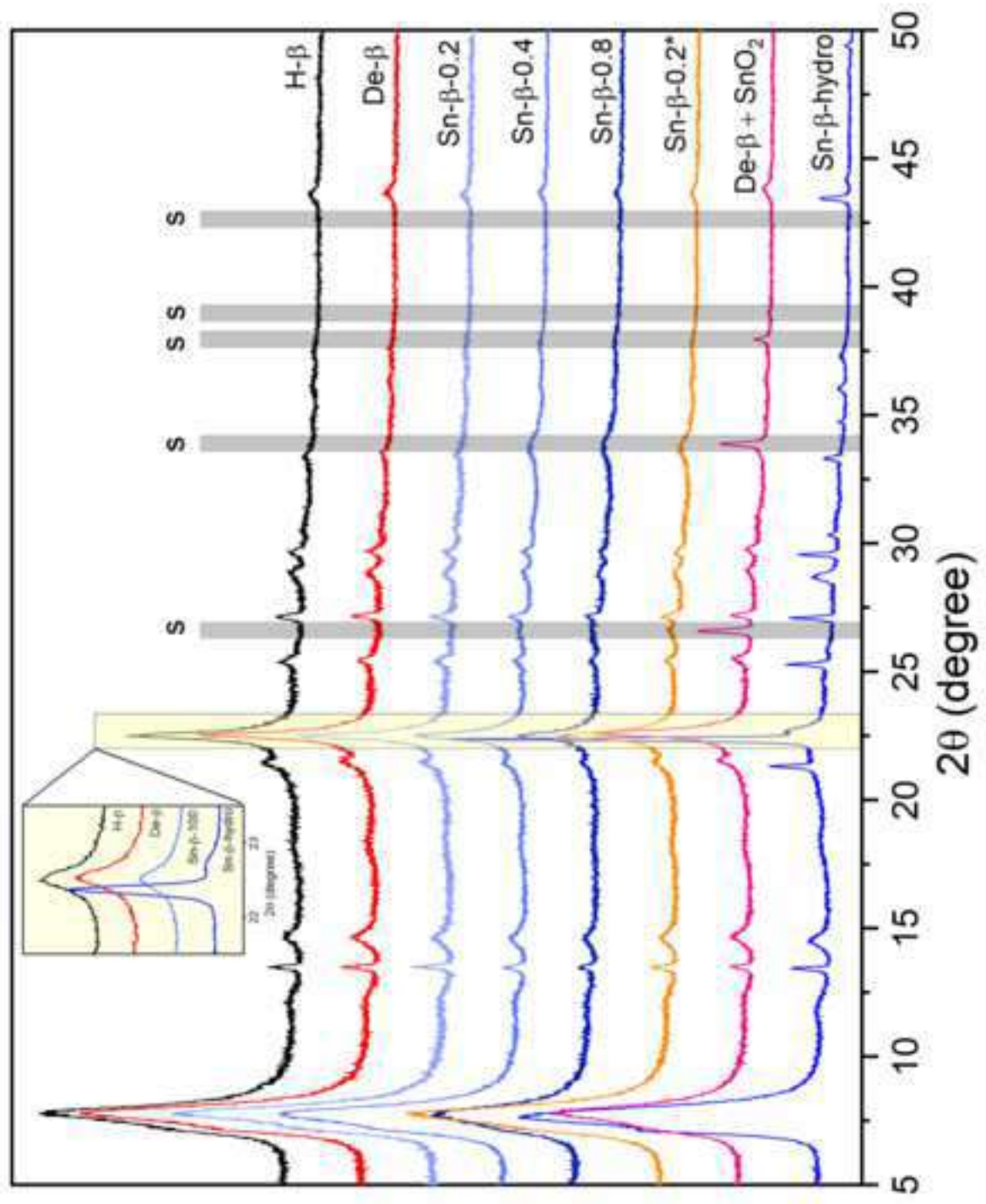




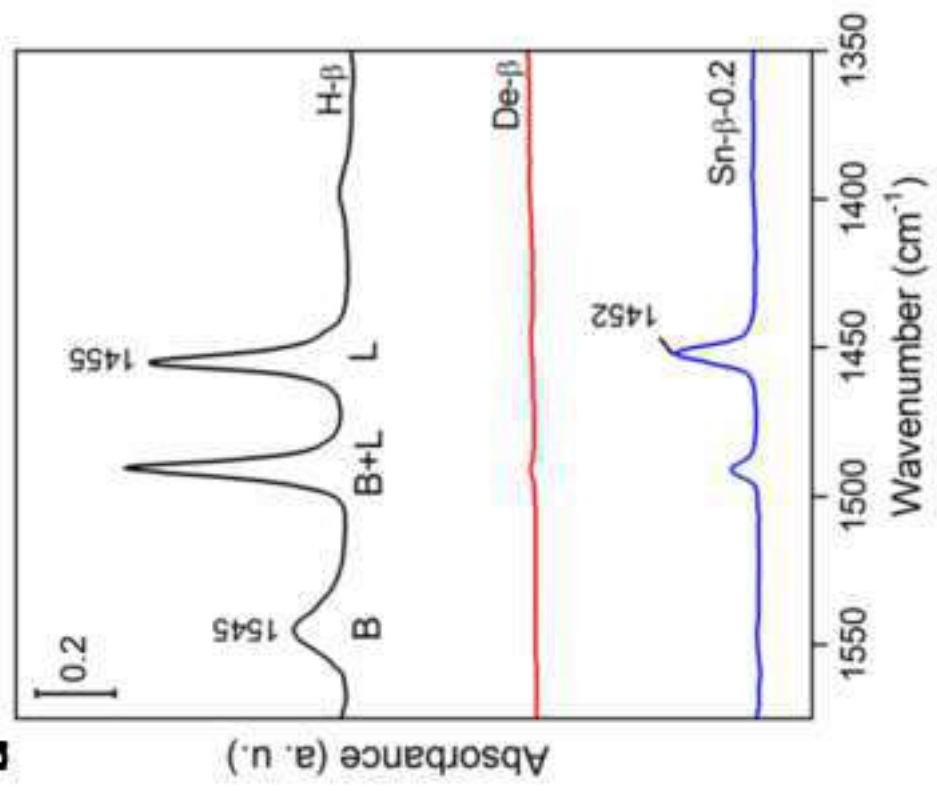








**a**



**b**

